Low-density diamondlike amorphous carbon at nanostructured metal-diamond interfaces

Brendan McBennett,[1,*,†] Yuka Esashi,[1,*] Nicholas W. Jenkins,[1] Albert Beardo,[1] Yunzhe Shao,[1] Emma E. Nelson,[1] Theodore H. Culman,[1] Begoña Abad,[1,‡] Michael Tanksalvala,[1,§] Travis D. Frazer,[1,‖] Samuel Marks,[2] Weilun Chao,[3] Sadegh Yazdi,[4] Joshua L. Knobloch,[1] Henry C. Kapteyn,[1,5] and Margaret M. Murnane[1]

[1]*Department of Physics, JILA, and STROBE NSF Science and Technology Center, University of Colorado and NIST, Boulder, Colorado 80309, USA*

[2]*Materials Science and Engineering, University of Colorado Boulder, Boulder, Colorado 80309, USA*

[3]*Center for X-Ray Optics, Lawrence Berkeley National Laboratory, Berkeley, California 94720, USA*

[4]*Renewable and Sustainable Energy Institute and the Materials Science & Engineering Program, University of Colorado, Boulder, Colorado 80309, USA*

[5]*KMLabs Inc., 4775 Walnut Street #102, Boulder, Colorado 80309, USA*

(Received 3 May 2024; accepted 13 August 2024; published 16 September 2024)

Next-generation nanoelectronic, energy, and quantum technologies require increasingly stringent thermal, optical, mechanical, and electrical properties of component materials, often surpassing the limits of widely used materials such as silicon. Diamond, an ultrawide bandgap semiconductor, is a promising material for these applications because of its very high stiffness, thermal conductivity, and electron mobility. However, incorporating diamond into devices that require high-quality metal-diamond interfaces is challenging. In this work, we use a suite of electron microscopy measurements to reveal an ultrathin amorphous carbon layer that emerges at metal-diamond interfaces after electron beam lithography. Using extreme ultraviolet scatterometry, we nondestructively determine lower bounds on the layer's Young's modulus and thermal conductivity, which at >230 GPa and >1.1 W/(m K) are indicative of a diamondlike form of amorphous carbon with high sp^3 bonding. However, extreme ultraviolet coherent diffractive imaging reflectometry and energy-dispersive x-ray spectroscopy measurements indicate a low and likely inhomogeneous density in the range of 1–2 g/cm^3. The low density of such a stiff and conductive layer could indicate that it contains nanometer-scale voids or atomic-scale vacancies. The appearance of this unusual layer illustrates the nanofabrication challenges for diamond and highlights the need for better techniques to characterize surfaces and interfaces in nanoscale devices.

DOI: 10.1103/PhysRevMaterials.8.096001

I. INTRODUCTION

Critical next-generation electronic and energy-efficient technologies—including advanced communications, computational systems, and electric vehicles—demand higher power devices with faster switching speeds [1]. However, the material property requirements for these devices often surpass the fundamental limits of widely used materials including silicon, motivating the need for better component materials. Diamond, an ultrawide bandgap semiconductor, is a material of great interest for advanced radio frequency and power electronics applications, because it exhibits higher dielectric breakdown strength, carrier mobility, thermal conductivity, and stiffness, beyond most other bulk materials [2–4]. Recent work has demonstrated that diamond is a promising material for advanced field-effect transistors [5,6]. Moreover, its high optical transmission makes it suitable for low-loss photonic circuits [7], while the luminescence from nitrogen-vacancy centers in diamond can be used for precise chemical, temperature, strain, and electromagnetic field sensors [8] as well as photon-based quantum communication and memory devices [9–11].

Single-crystal diamond can be produced in high-quality bulk form, but poses many nanofabrication challenges, limiting its integration into devices. Many nanoelectronic and quantum applications require that structures are fabricated either on or into diamond [12], that the doping and termination of diamond is precisely controlled [1,2], and that nitrogen-vacancy centers are induced through ion implantation. However, due to diamond's hardness and resistance to many chemical etchants, it is challenging to polish, structure, or locally dope. At the same time, diamond is not immune to surface damage and contamination [12,13]; for example, the ion implantation process for the creation of nitrogen-vacancy centers is known to produce a graphitic layer on diamond. While this layer can be removed with an acid cleaning of exposed diamond surfaces [14–16], such treatments can be difficult to incorporate into fabrication procedures for multilayers, heterostructures, or metallic contacts that are required for nanoelectronics and resonators [17]. Moreover, high-quality interfaces are essential to leveraging diamond's advantageous properties, e.g., minimizing interfacial thermal

*These authors contributed equally to this work.

†Contact author: brendan.mcbennett@colorado.edu

‡Present address: Physics Department, University of Basel, Klingelbergstrasse 82, CH-4056 Basel, Switzerland.

§Present address: National Institute of Standards and Technology (NIST), Boulder, Colorado 80305, USA.

‖Present address: KMLabs Inc., 4775 Walnut St. #102, Boulder, Colorado 80309, USA.

resistance is essential for diamond to act as an effective heat sink [18]. Therefore, it is critical to understand and mitigate the amorphization of surfaces and interfaces for the effective application of diamond in nanoscale devices.

Amorphous carbon exhibits a wide range of material properties due to the variety of nanoscale topologies and chemical bonds that it can adopt [19–21]. Over the last three decades, the discovery and characterization of different forms of amorphous carbon has been the subject of extensive efforts. Densities have been measured using electron energy loss spectroscopy [22–27], x-ray reflectivity [21,27,28], Rutherford backscattering [22,23,29], and by measuring implanted dopant density using secondary ion mass spectrometry [29]. Elastic properties have been measured using ultrasonic surface waves [30,31], surface Brillouin scattering [32,33], and nanoindentation [21]. Finally, the thermal conductivity has been measured using laser pump-probe techniques [34] and the 3ω method [35,36]. Many of these techniques have spatial resolutions of $>100\,\mu$m, making them unsuitable for studying properties on or around individual nanostructures. Some also risk damaging the sample due to high-energy electrons or charging effects, or require destructive sample preparation or milling. Moreover, it is challenging to extract the elastic properties of ultrathin films with thicknesses $\ll$100 nm, or of films around nanostructures, using standard ultrasonic and nanoindentation techniques, although surface Brillouin scattering has characterized carbon films on the 10 nm scale [37].

In this study, we use electron beam lithography to fabricate nanoscale one-dimensional (1D) nickel gratings on a single-crystal diamond substrate. Initial measurements of this sample using extreme ultraviolet probes led us to suspect fabrication-induced materials modification. To investigate this, we used cross-sectional scanning transmission electron microscopy, electron energy loss spectroscopy, and energy-dispersive x-ray spectroscopy and detected an amorphous carbon layer that is $\sim$5 nm thick underneath the nickel structures and $\sim$20 nm thick between the nickel structures. This layer is not present on the diamond substrate before fabrication and appears across multiple fabrications with modified recipes. Its presence complicates heat exchange across the metal-diamond interface, and illustrates the challenge of incorporating diamond into established device-relevant fabrication procedures.

To characterize the material properties of the amorphous carbon layer and investigate its potential impact on the functionality of diamond-based nanoelectronics, we use extreme ultraviolet (EUV) coherent diffractive imaging reflectometry and energy-dispersive x-ray spectroscopy (EDS) to measure the density, and dynamic EUV scatterometry to measure the Young's modulus and thermal conductivity [38–40]. Coherent EUV light is an ultrasensitive, nondestructive probe of the properties of nanoscale layers and structures. EUV imaging reflectometry has compositional specificity and can perform quantitative, nondestructive measurement of thin layers and nanostructures at high spatial resolution [39,40]. Dynamic EUV scatterometry is insensitive to valence electron dynamics, making it well suited for the investigation of thermal and mechanical behaviors on length scales far below the visible diffraction limit, and on subpicosecond timescales [41–43].

The EUV imaging reflectometry and EDS techniques measure an amorphous carbon density of 1.0 ± 0.3 g/cm^3 and 1.8 g/cm^3, respectively. The different values obtained by these local measurements suggest that the amorphous layer exhibits heterogeneous properties. A further wide-area characterization of density using x-ray reflectivity (XRR) estimates a density of $\sim$1.8 g/cm^3. Despite the relatively low density, the EUV scatterometry dataset is only consistent with an amorphous carbon Young's modulus >230 GPa and thermal conductivity $>1.1\,\mathrm{W/(m\,K)}$, values more characteristic of a higher-density diamondlike form of amorphous carbon. The thin amorphous carbon layer may therefore contain irregular nanometer- or subnanometer-scale voids or vacancies, or be affected by the properties of the diamond underneath. The repeated observation of this amorphous carbon layer in multiple electron-beam lithography processes involving metal deposition and liftoff foreshadows the challenges of incorporating single-crystal diamond into complex device-relevant fabrication recipes, where interfacial defects between the diamond and active layer can bottleneck heat evacuation.

II. AMORPHOUS CARBON LAYER ORIGIN AND CHARACTERIZATION

The amorphous carbon layer appears both underneath and between 1D nickel gratings of varying linewidth (L) and period (P), which are fabricated using a standard electron-beam lithography process. The diamond substrates are first cleaned in a boiling mixture of sulfuric and nitric acids to ensure minimal contamination is present before the process begins, which was verified by the XRR measurements in Supplemental Material (SM) Sec. I [44]. A 50-nm spin-coated layer of polymethyl methacrylate (PMMA) serves as the positive resist, and a 15-nm evaporated aluminum layer mitigates charging effects from the electron beam. Two variants of the process use different electron energies (30 vs 100 keV) and metal deposition techniques (thermal vs electron-beam evaporation), but result in a similar amorphous carbon layer. After exposure, removal of the aluminum layer and development of the PMMA, an $\sim$12-nm nickel layer is deposited between and on top of the remaining PMMA. A liftoff step removes the remaining PMMA, transferring the lithographic pattern to the nickel. SM Sec. I contains additional details on the diamond substrates and step-by-step fabrication recipes [44].

Initial measurements of this sample using EUV probes suggested fabrication-induced materials modification. The presence of an amorphous layer was then detected using scanning transmission electron microscopy. As illustrated in Fig. 1(b), the amorphous carbon (dark red) is thicker between the nickel structures than underneath, corresponding to a modulation in the height of the diamond substrate itself. This suggests that the nickel structures played a role in the amorphous carbon layer's formation. However, as discussed in SM Sec. I, individual fabrication steps, in isolation, are likely insufficient to produce the amorphous layer, suggesting that it arose from a combination of factors, and complicating the development of an alternative recipe [44]. Figure 1(a) shows a high-resolution image of the amorphous layer, obtained using high-angle annular dark-field scanning transmission electron microscopy (HAADF-STEM), which requires the preparation, via focused ion beam milling, of a thin lamella, in this case from the area of the sample covered by the nickel

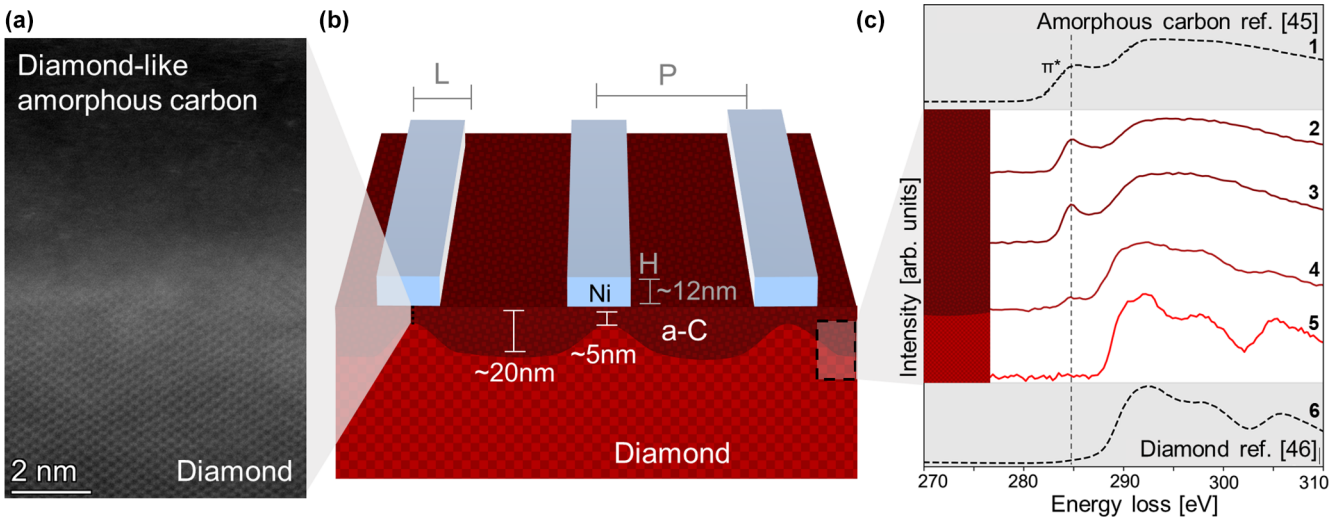

FIG. 1. Amorphous carbon layer that forms on diamond after electron-beam lithography. (a) HAADF-STEM image of the amorphous carbon layer between a nickel structure and the diamond substrate, illustrating a lack of crystallinity. (b) Schematic of the 1D nickel grating of linewidth (L), period (P), and height (H, ∼12 nm), with labeled approximate amorphous carbon dimensions. (c) EELS characterization of the amorphous carbon layer. Spectra 2 and 3 show variation within the amorphous carbon layer in the cross-plane direction, while spectrum 4 is averaged across the smooth interface between the amorphous carbon and diamond. Spectrum 5 is taken in the crystalline diamond substrate. Spectra 1 and 6 are references of amorphous carbon and diamond, respectively [45,46]. The peak at 284.5 eV indicates the π^* bonding characteristic of sp^2 hybridization.

grating of linewidth $L = 50$ nm and period $P = 200$ nm. The crystallinity of the diamond substrate is evident. Because the HAADF imaging only records inelastically scattered electrons, the relative darkness of the amorphous carbon indicates a lower density than diamond. A second lamella, extracted a millimeter-scale distance from the first, exhibits a similar amorphous layer between two nickel structures in the larger $L = 6$ μm, $P = 8$ μm grating geometry. Electron energy loss spectroscopy (EELS) spectra obtained at this location and shown in Fig. 1(c) provide evidence that the amorphous carbon originated from the diamond substrate and contains a mixture of sp^2 and sp^3 bonding. No oxygen was detected inside the amorphous carbon layer, indicating that it is not a cross-linked or polymerlike product of the PMMA resist. The EELS spectra were processed using HYPERSPY [47] and are shown as a function of sample depth. Inside the amorphous region, the spectra exhibit clear signatures of π^* bonding at 284.5 eV, sp^2 hybridization, and resemble literature measurements of a variety of amorphous carbons [20,27,45,48]. The π^* bonding exhibits a gradient across the amorphous layer, as illustrated by the differences between spectra 2–4, indicating that the sp^2 fraction decreases with film depth before disappearing across a smooth several-nanometer interface with the crystalline diamond [20].

The EDS measurements shown in Fig. 2 provide localized information on elemental composition and measure a low amorphous carbon density ranging from approximately 1.7 to 2.0 g/cm^3 across several measurements from two sample locations, with an average of 1.8 g/cm^3. Figure 2(b) displays the integrated intensity of the carbon peak across the blue and red boxes in Fig. 2(a), representing the bulk diamond and amorphous carbon layer, respectively. Notably, the carbon peak intensity drops by approximately 50% as one transitions from the bulk diamond region to the amorphous layer. The focused ion beam (FIB)-prepared transmission electron microscopy (TEM) sample maintains a uniform thickness across these regions, allowing for a direct correlation between the reduction in the intensity of the carbon peak and the low density of the amorphous layer. Assuming the amorphous layer comprises solely carbon, as confirmed by both EDS and EELS, the amorphous layer density can be deduced from the carbon peak ratio (details in SM Sec. II [44]). In this calculation, a diamond density of 3.5 g/cm^3 is employed, and instead of peak intensity, the area under the peak was integrated from Gaussian fitting and utilized for enhanced accuracy. The EDS image also includes aluminum and platinum layers, which are deposited to facilitate the TEM sample preparation. The oxygen present at the sample surface is likely due to the oxidation of the aluminum overlayer and nickel structure boundary. However, the oxide layer also extends underneath the nickel structure, where it is ∼3 nm thick. Since the nickel was deposited under vacuum, this suggests that some oxygen was present on the sample surface at that time, perhaps from residual PMMA or the natural oxygen termination of the diamond substrate.

To confirm that the amorphous carbon layer extends beyond the immediate vicinity of the nickel structures, which cover only a small fraction of the sample surface, we perform XRR measurements, as shown in Fig. 1 of the SM [44]. Because the x-ray beam averages over a millimeter-scale area at grazing angles, the interference fringes in the post-fabrication measurement indicate that the amorphous layer does likely extend over a wide area. The XRR data can be fit by a model consisting of a uniform ∼12-nm carbon layer of ∼1.8 g/cm^3 density on a diamond substrate (details in SM Sec. I [44]). For comparison, an XRR measurement of a diamond substrate prior to fabrication shows no trace of the amorphous carbon layer, confirming that it forms during the fabrication process.

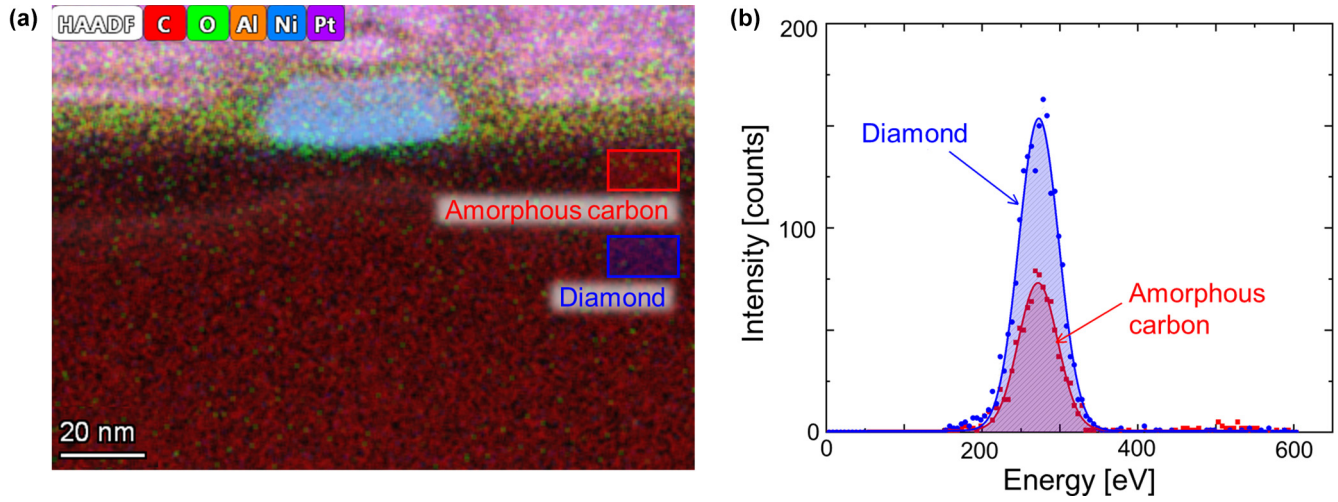

FIG. 2. Energy-dispersive x-ray spectroscopy measurements and density characterization. (a) EDS image showing elemental composition of a single nickel nanostructure and the area underneath. The amorphous carbon exhibits fewer carbon counts than the crystalline diamond, and is thinner beneath the nickel structures. (b) EDS characterization of the amorphous carbon density. The integrated intensity of the carbon peak in the amorphous layer (red) is approximately 50% of the crystalline diamond substrate (blue), indicating an amorphous carbon density of 1.8 g/cm^3.

III. EUV COHERENT DIFFRACTIVE IMAGING REFLECTOMETRY FOR MEASUREMENT OF AMORPHOUS CARBON DENSITY

EUV coherent diffractive imaging reflectometry is a technique that combines computational coherent diffractive imaging with reflectometry to measure the geometry and composition of nanostructures in a spatially resolved way [39,40]. A similar technique, EUV reflectometry, measures specular reflectivity as a function of incidence angle, and it has previously been used to study amorphous carbon [49]. Coherent diffractive imaging reflectometry differs in that it can operate on and around nonperiodic structures, and also gain information from the phase-upon-reflection of the reflected EUV light, in addition to the reflected intensity.

In order to determine the density of the surface amorphous carbon layer, the corner of a single nickel structure in a grating with linewidth $L = 6$ μm and period $P = 8$ μm was computationally imaged using coherent EUV ptychography [50–53] at incidence angles between 19° and 29° from grazing. The data collection for a single image involved recording coherent diffraction patterns from the sample at overlapping beam positions using an EUV beam of 29.4-nm wavelength, which is produced via high harmonic generation and focused to a few-micron spot on the sample. This process was repeated at each of the incidence angles. A more detailed description of the experimental setup and procedure can be found in Refs. [39,40] and SM Sec. IV [44].

The stack of diffraction patterns at each angle was fed into a ptychography algorithm to form real-space images of the sample. The images quantitatively map the complex (i.e., phase and amplitude) reflectivity across the field of view. The phase images that were used in the analysis are shown in Fig. 3(a). These images were then registered onto each other, and a set of pixels was selected, as indicated in the 19° image in Fig. 3(a), to measure the average phase step between regions on and off the nickel structures at each incidence angle. The resultant phase step curve is shown as the black data points in Fig. 3(b), with small error bars as indicated.

Extraction of the amorphous carbon density from the phase step vs incidence angle curve is an inverse problem; thus, we fit a sample model whose theoretically calculated phase step curve matches the experimental measurement. The theoretical calculation of the phase step curve was achieved by modeling the depth-dependent composition of the sample using the parameters in Table I of the SM, for regions on and off the nickel structure, using the Parratt formalism [44,54] to calculate the complex reflectivity in the two regions. The Parratt formalism is an appropriate method to use for the prediction of complex reflectivity when the object is composed of multiple layers as it properly accounts for the presence of multiple interfaces. The optimization of the model was performed using a genetic algorithm [55,56]. Once a model that fits the experimental data was found, confidence intervals on the fitted parameters were calculated using the diagonal elements of the covariance matrix [39,40,57].

Two sample parameters were floated when fitting a sample model with the genetic algorithm: the amorphous carbon density and the nickel structure height. The structure height was floated only within the confidence interval of atomic force microscopy measurements described in SM Sec. III [44]. In addition to the sample parameters, experimental parameters, including the deposition rate of hydrocarbon contamination in the two regions due to the high-energy EUV photons and slight offsets in the incidence angle and the wavelength were also floated. The amorphous carbon density was solved to be 1.0 ± 0.3 g/cm^3 (see SM Sec. IV for details on error analysis and uncertainty [44]). The different EUV imaging reflectometry, EDS, and XRR density measurements could indicate that localized areas of exceptionally low density, such as that measured by the EUV imaging reflectometry, contribute to a low average density of the amorphous carbon. In the following sections we show that regardless of the exact average density value, the amorphous carbon layer exhibits

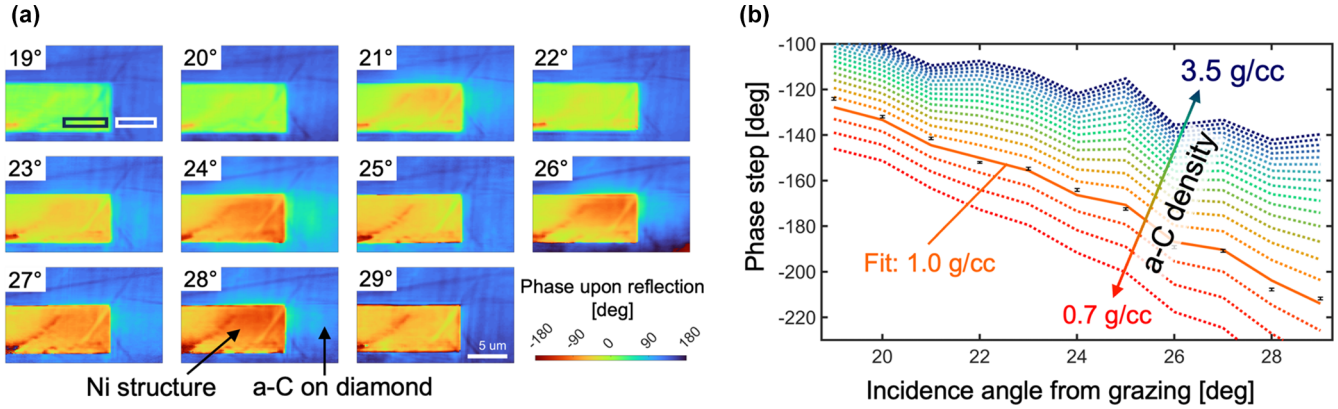

FIG. 3. EUV imaging reflectometry to measure the density of the surface amorphous carbon layer. (a) Eleven ptychographic reconstructions of a nickel nanostructure on the sample, shown in phase-upon-reflection. The black and white rectangles in the 19° image show the pixels that were selected from regions on and off the nickel structure, respectively, when calculating the phase step. The change in contrast between the nickel structure and substrate across the 11 images is due to the changing complex reflectivity of EUV light as a function of incidence angle (the signal of interest in this technique), as well as a slight hydrocarbon contamination build up over the course of the data collection. (b) Black data points (including error bars) show the phase step between regions on and off the nickel structure as a function of incidence angle from grazing. The dotted lines show the fitted theoretical phase curves for different densities of the amorphous carbon layer, between 0.7 and 3.5 g/cm^3 in 0.1-g/cm^3 increments. The solid line shows the best fit curve at a density of 1.0 g/cm^3.

elastic and thermal properties characteristic of a diamondlike material.

IV. DYNAMIC EUV SCATTEROMETRY: ACOUSTICS ANALYSIS FOR MEASUREMENT OF YOUNG'S MODULUS AND STRAIN COEFFICIENT

To investigate the thermal and elastic properties of the amorphous carbon layer, we use an EUV scatterometry experiment to monitor sample surface displacement as a function of time delay after its excitation by infrared pulses from a 4 kHz, ∼25 fs Ti:sapphire amplifier (KMLabs). The initial excitation is primarily confined to the nickel grating due to the bandgap of the diamond substrate, but fully dissipates into the substrate during the 250 s pulse interval. At some time delay relative to the infrared pump, a coherent EUV probe pulse upconverted from the infrared via high harmonic generation diffracts from the perturbed nickel grating and onto a CCD camera. Summing the difference between the perturbed and static EUV diffraction patterns across the camera frame at a series of pump-probe time delays yields the experimental signal shown in Fig. 4. The 40–50-eV EUV photons are insensitive to the valence electron dynamics that dominate visible transient reflectivity signals and instead mainly monitor sample surface displacement due to thermal expansion and acoustic oscillations [41]. Further details on the present dynamic EUV scatterometry experiment appear in Refs. [38,43] where it was used to characterize the properties of ultrathin films and nanoscale heat flow.

As shown in Fig. 4, the experimental signal resolves a longitudinal acoustic wave (LAW) propagating in the nickel grating on the picosecond timescale (blue) and a surface acoustic wave (SAW) propagating along the substrate surface on the nanosecond timescale (black). These hypersonic acoustic waves result from the impulsive excitation of the nickel grating by an ultrafast pulse and have wavelengths set by the grating height and period, respectively. The penetration depth of the SAW energy into the carbon layer and diamond substrate is determined by its wavelength, providing depth sensitivity controlled by the grating period. For SAWs of long wavelength (λ_{SAW}) launched by large period laser-excited gratings, the acoustic energy penetrates deep into the sample ($\sim\lambda_{SAW}/\pi$) and is predominantly sensitive to the substrate density and elastic properties. For short-wavelength SAWs launched by small period gratings, the acoustic energy is more confined in the amorphous carbon layer and is predominantly sensitive to its elastic properties. In addition to the acoustic oscillations, a thermal decay (red) appears in Fig. 4, corresponding to the gradual relaxation of the nickel structures to their nominal heights via the release of incoherent thermal phonons into the substrate below, as analyzed in Sec. V.

In Fig. 5(a), we plot the experimentally measured SAW dispersion, shown by the magenta squares and corresponding error bars. The SAW velocity is the measured frequency (extracted via a chirp Z transform [42]) multiplied by the grating period, i.e., SAW wavelength. To predict the SAW dispersion, we constructed a finite element model of one unit cell of the grating-substrate stack using the commercial software COMSOL [58] (details in SM Sec. V [44]). We utilize an eigenfrequency calculation paired with the SAW-likeness metric and spectral decomposition approach used in Refs. [59,60] to predict the SAW frequency as a function of the grating period. If we include only a diamond substrate beneath the nickel structures, using literature values for material properties and nanostructure dimensions measured by atomic force microscopy, we predict the gray dots shown in Fig. 5(a). We find that this curve agrees well for large SAW penetration depths, indicating a primary sensitivity to only the diamond substrate for micron-scale SAW wavelengths. However, for the smallest SAW wavelength ($\lambda_{SAW} = 200$ nm), the measured velocity deviates significantly from the diamond substrate calculation due to the presence of the amorphous carbon layer.

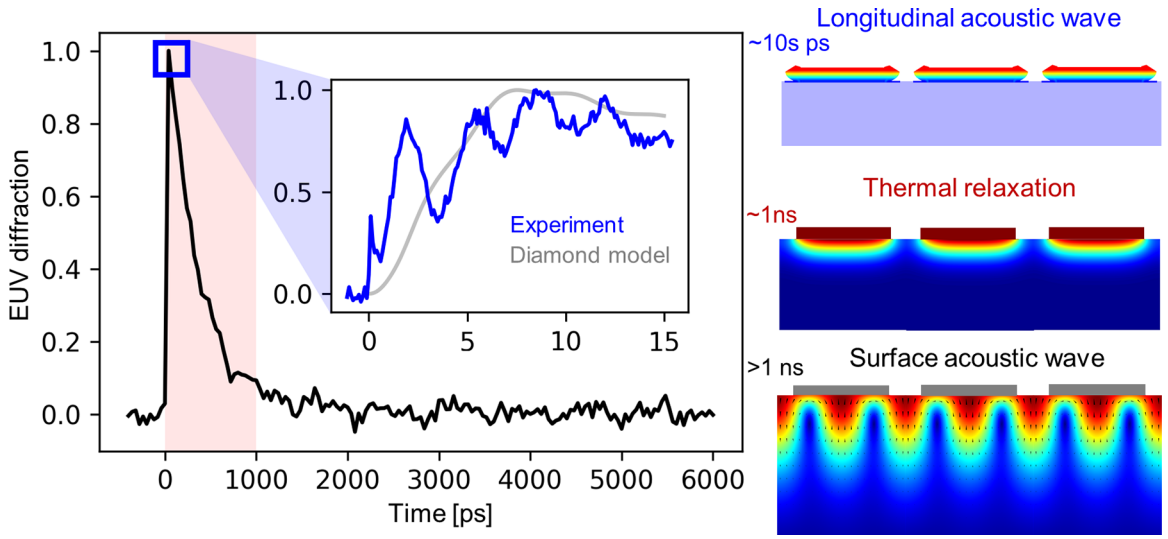

FIG. 4. Dynamic EUV scatterometry data for acoustic and thermal analysis. After an ~25-fs infrared pump laser excites the nickel grating, diffraction by a time-delayed EUV probe pulse reveals dynamics on multiple timescales, including longitudinal acoustic waves propagating in the nickel grating (blue), surface acoustic waves propagating in the substrate (black), and heat flowing from the nickel structures into the substrate (red shading). The inset also shows a finite element simulation (gray) of the short-timescale dynamics for a Ni-diamond interface without amorphous carbon, which does not exhibit acoustic oscillations. All data and simulations are for an $L = 6\,\mu\text{m}$, $P = 8\,\mu\text{m}$ nickel grating. The schematics on the right show snapshots from finite element simulations of the deformation or temperature for the acoustic waves and thermal relaxation, respectively, at the indicated timescales.

By adding the more compliant amorphous carbon and oxide layers observed in the HAADF-STEM and EDS measurements to the finite element model, we fit the data, which allows us to extract the elastic properties of the amorphous carbon. Within the finite element model, we set the amorphous carbon layer density to the value measured by EUV imaging reflectometry or EDS. We vary the amorphous carbon Young's modulus until the simulations reproduce the experimentally measured SAW frequency for the smallest grating periodicity. With the extracted value of Young's modulus, we can compute the predicted SAW velocity across all grating sizes. An example of a fitted SAW dispersion for an amorphous carbon density of 1.0 g/cm^3 is shown by the green triangles in Fig. 5(a) and agrees well with the measured SAW dispersion. Details on the experimental analysis, model, input parameters, validations, and our error bar calculations via stochastic modeling methods are found in SM Secs. V and VI [44]. We cannot independently extract both the Young's modulus and the Poisson's ratio with only a single acoustic wave velocity. However, previous studies indicate that amorphous carbon typically has a Poisson's ratio within a specific range. Diamondlike tetrahedral carbon with predominantly

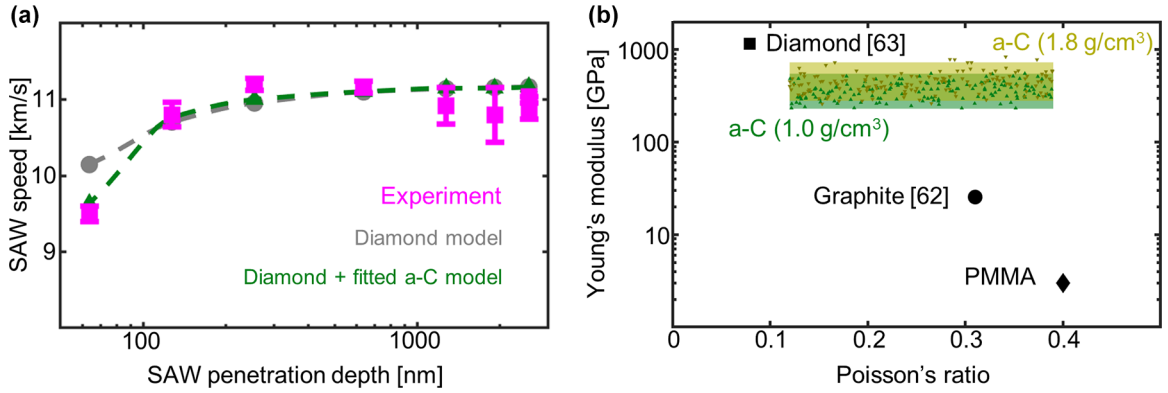

FIG. 5. Amorphous carbon layer elastic properties. (a) Experimentally measured SAW velocity as a function of the penetration depth set by the nickel grating period (magenta squares). The gray dots show finite element predictions for a purely diamond substrate, while the green triangles show an example finite element fit for a 1.0 g/cm^3 structured amorphous carbon layer on a nominal diamond substrate. The green solid and gray dashed lines are guides to the eye. (b) The region of fitted elastic properties, i.e., Young's modulus and Poisson's ratio, for the amorphous carbon layer for the two densities measured by EUV imaging reflectometry (green) and EDS (yellow), in comparison to literature values for graphite [62], diamond [63], and PMMA. Because the Poisson's ratio is unknown, the extracted value of the Young's modulus is shown as a function of an assumed Poisson's ratio which has been randomly sampled. The shaded regions indicate the Young's modulus 95% confidence bounds.

sp^3 bonding can have a Poisson's ratio as low as 0.12, while hydrogenated amorphous carbon can have a Poisson's ratio around 0.39 [32,33,61]. In Fig. 5(b), we plot the range of possible Young's moduli as a function of the assumed Poisson's ratio which was randomly sampled for a density of both 1.0 and 1.8 g/cm^3. For the lower density extracted by EUV imaging reflectometry, we find that Young's modulus is in the range 230–550 GPa; while for the higher density extracted by EDS, we find a Young's modulus range of 280–730 GPa. Thus, the amorphous carbon is impressively stiff, with a Young's modulus >230 GPa, especially considering its low density.

The strong oscillations of the LAWs propagating within the gratings provide further evidence of the extensive amorphous carbon layer, as illustrated in the Fig. 4 inset. Using a finite element model of the $L = 6$ μm, $P = 8$ μm nickel grating incorporating a pristine Ni-diamond interface without any amorphous carbon, we calculate the time-dependent surface deformation on sub-100-ps timescales and model the corresponding EUV diffraction signal, which we compare to the experimental data. Interestingly, we find that this simulation (gray curve) cannot reproduce the experimental data (blue curve), even when incorporating an NiO layer with nominal properties. The similar acoustic impedances between the Ni, NiO, and diamond causes the LAW energy to rapidly escape and strong oscillations are not observed in the simulation. However, the strong oscillations clearly present in the experiment are identical for all measured grating geometries (details in SM Sec. V [44]). These results indicate that the interface between Ni and diamond has been significantly modified such that the acoustic impedance is quite poor across the entire sample.

V. DYNAMIC EUV SCATTEROMETRY: THERMAL ANALYSIS

The thermal decay in the EUV scatterometry data can be analyzed using the finite element model introduced in Sec. IV to determine a lower bound on the thermal conductivity of the amorphous carbon layer. By solving the heat equation coupled to the linear elastic equation in the time domain within the full sample geometry, we calculate the phonon temperature evolution and thermal expansion over the 1.5 ns following the infrared pump excitation. Neglecting ultrafast electron dynamics, the simulation begins with the injection of a spatially uniform energy density into the nickel structure of the form $\mathcal{Q}(t) = \mathcal{Q}_0 e^{-t/\tau_{ep}}$, where $\tau_{ep} = 450$ fs is the approximate equilibration timescale for the electron and phonon temperatures in nickel after excitation by an ultrafast laser [64]. Because of the large size of the nickel grating considered here ($L = 6$ μm, $P = 8$ μm) relative to the thermal phonon mean free paths in diamond, nanoscale thermal transport effects need not be considered [65]. A Fresnel diffraction simulation translates the simulated thermal expansion into an EUV diffraction pattern, which can be compared directly to the experimental signal (details in SM Sec. V [44]). At visible laser wavelengths, the variable optical properties of amorphous carbon complicate interpretation of the diffraction signal and would also influence the performance of diamond-based quantum sensing devices [66]. However, because the thermal expansion of the nickel structures dominates the EUV diffraction signal, the present analysis is only minimally sensitive to uncertainties in the exact amorphous carbon optical properties [41].

Due to diamond's very high thermal conductivity, heat will spread quickly once it reaches the substrate. However, interfacial thermal resistance is often the main constraint on heat evacuation in semiconducting devices. The oxide and amorphous carbon layers shown in Fig. 1, along with the interfaces between layers, present a modified thermal boundary resistance (TBR) between the heated nickel structures and the diamond substrate. This TBR is the ratio of the temperature drop between the nickel and diamond and heat flux leaving the nickel, and bottlenecks the thermal relaxation of the nickel structures [67]. The total TBR between the nickel and diamond can be expressed as a sum in a series of individual resistances, $R = R_{NiO} + R_{a\text{-}C} + R_{Int}$, where R_{NiO} and $R_{a\text{-}C}$ are the resistances associated with the oxide and amorphous carbon layers, respectively, and are functions of their thicknesses and thermal conductivities, κ_{NiO} and $\kappa_{a\text{-}C}$. The final term, R_{Int}, accounts for interfacial TBR between the various layers. By fixing values for all variables except $\kappa_{a\text{-}C}$ in the finite element model described above, we can in principle determine the value of $\kappa_{a\text{-}C}$ that best matches the experimental data. The amorphous carbon and oxide thicknesses can be extracted from the electron microscopy data, while κ_{NiO} is set to its bulk value of 35 W/(m K) (details in SM Sec. III [44]). The amorphous carbon density does not significantly impact the results, which are similar if it is set to 1.0 or 1.8 g/cm^3. However, the interfacial TBR represented by R_{Int} is highly dependent on the fabrication process and in the present experiment its value cannot be measured independently of $\kappa_{a\text{-}C}$ [18].

Instead, by setting R_{Int} to a physical lower bound, it is possible to determine a lower bound on $\kappa_{a\text{-}C}$. The minimum physical TBR at a material interface is determined by assuming that the internal energy fluxes are perfectly transmitted across the interface [68]. For an isotropic, near-equilibrium crystalline material, assuming phonon-dominated interface conductance and Debye phonon dispersion relations, this limit is set by phonon flux incident on an arbitrary crystallographic plane and can be expressed as [69]

$$R_{Int} \geqslant \left[\frac{1}{4} \sum_j \int_0^{\omega_j^{max}} \hbar \omega v_j D_j(\omega) \frac{\partial f_0(\omega, T)}{\partial T} d\omega \right]^{-1} \simeq \frac{4}{c_V v_g}, \tag{1}$$

where ω_j^{max} and v_j are the Debye frequency and group velocity for phonons with polarization j, v_g is the average phonon group velocity, $f_0(\omega, T)$ is the Bose-Einstein distribution function, $D_j(\omega)$ is the density of states, and c_V is the volumetric heat capacity. Since the materials on either side of an interface have different internal energy fluxes, the less conductive material determines the minimum physical TBR for a particular material pair [69]. We therefore insert nickel material properties on the right-hand side of Eq. (1), resulting in the bound $R_{Int} \geqslant 0.3$ nK m^2/W.

Accordingly, a lower limit on the amorphous carbon thermal conductivity can be calculated as $\kappa_{a\text{-}C} \geqslant 1.1$ W/(m K). This is accomplished by varying sensitive parameters in the finite element and diffraction simulations, such as nickel

structure height and amorphous carbon thickness, within their uncertainties to achieve the minimum $\kappa_{a\text{-}C}$ fit (details in SM Sec. VI [44]). We stress that this value is a bound rather than an estimation of the actual amorphous carbon thermal conductivity, since experimentally measured interfacial TBRs are generally much higher than the lower bound given by Eq. (1). If we instead set $R_{Int} = 3.3$ nK m^2/W based on recent measurements of nickel-diamond interfaces [70], the fitted value of $\kappa_{a\text{-}C}$ rises to 2.8 W/(m K). Moreover, the 35 W/(m K) used for κ_{NiO} may be an overestimate, since the oxygen underneath the nickel structures in the EDS measurement may also indicate the presence of leftover PMMA. However, a reduction in κ_{NiO} in the model will only increase the lower bound on $\kappa_{a\text{-}C}$. We note that an amorphous carbon thermal conductivity above ∼1 W/(m K) excludes a large class of hydrogenated and polymerlike carbon materials, which generally have far lower thermal conductivities [35,36], and Young's moduli, as discussed above.

VI. DISCUSSION

The various manifestations of amorphous carbon are often classified according to their sp^3 bonding ratio and hydrogenation, where high sp^3 ratios and low hydrogen contents correspond to tetrahedral amorphous carbons, with higher density, thermal conductivity, and stiffness relative to sp^2-dominated (graphitic) and hydrogenated forms of amorphous carbon [21]. Within this framework, the present amorphous carbon film is anomalous. A density of 1.8 g/cm^3 is characteristic of a graphitic or hydrogenated material, while a density of 1.0 g/cm^3 corresponds to a polymerlike material. However, a thermal conductivity above 1.1 W/(m K) and Young's modulus above 230 GPa suggest the higher sp^3 bonding and low hydrogen content typical of tetrahedral amorphous carbon. Figure 6 compares the thermal conductivities and Young's moduli predicted and observed for various amorphous carbons as a function of density. As shown in Fig. 6(a), the low thermal conductivities of bulk forms of hydrogenated and graphitic amorphous carbons with densities below 2.0 g/cm^3 are incompatible with the present amorphous layer. While simulations of graphitic amorphous carbon with densities near 1.8 g/cm^3 (gold circles) can exhibit similar Young's moduli to the present layer [71], experimentally measured stiffnesses of amorphous carbon films at this density are lower [30,36]. The combination of low density, high stiffness, and high conductivity observed here is therefore indicative of a porous structure with a relatively stiff and conductive constituent material. Because the amorphous carbon film is so thin, any porous structure would necessarily consist of highly irregular voids and vacancies at nanometer or subnanometer scale, with the constituent material exhibiting a mixture of sp^2 and sp^3 bonding, as suggested by the EELS characterization. Small, irregular pores in amorphous materials are difficult to image using projective electron microscopy techniques such as HAADF-STEM, but might be resolved in future work using atomistic tomography methods [72]. Variations in the density measured by EDS, XRR, and EUV imaging reflectometry could be explained by a spatially inhomogeneous distribution of pores and vacancies, since each technique averages over a different length scale, from nanometers in the case of EDS to microns and millimeters for EUV imaging reflectometry and XRR, respectively. Variations between the techniques might also relate to differences in how each metrology technique interacts with an irregular, nanoporous surface, which is first coated in metal in the case of EDS, but exposed in the XRR and EUV measurements.

In porous carbon, stiffness has been shown to increase with decreasing pore size, enabling nanoporous amorphous materials to exhibit exceptionally high Young's moduli not attainable in macroscopic structures [81]. For example, while millimeter- and micron-scale porous carbon structures exhibit Young's moduli in the megapascal range [82], nanoscale pyrolytic carbon architectures can achieve Young's moduli up to 20 GPa at densities below 1 g/cm^3 [83]. The stiffness of these cellular metamaterials is often compared to the Hashin-Shtrikman upper bound on the effective Young's modulus of a quasi-isotropic, quasi-homogeneous porous material [84],

$$\frac{E_{eff}}{E_0} \leqslant \frac{2\bar{\rho}(7-5\nu)}{15(\bar{\rho}-1)\nu^2 + 2(\bar{\rho}-6)\nu - 13\bar{\rho} + 27}, \qquad (2)$$

where $\bar{\rho}$ is the filling fraction (one minus the porosity), and E_0 and ν are the bulk Young's modulus and Poisson's ratio of the constituent material. As shown in Fig. 6(b), the Young's modulus of the present amorphous layer characterized in Sec. IV slightly exceeds the Hashin-Shtrikman bound, even for the 1.8 g/cm^3 density and assuming diamond as the constituent material to maximize the right-hand side of Eq. (2).

The high stiffness of this amorphous layer is in line with recent progress in atomistic simulations of thermodynamically stable forms of amorphous carbon [76,85–87], some of which are shown to accommodate both nanoscale porosity and a significant fraction of sp^3 bonding. While the porosity of the present layer is unknown, recent simulations of 50% porous amorphous carbon with densities near 1 g/cm^3 show Young's moduli near 200 GPa [orange stars in Fig. 6(b)], consistent with the present experimental observations [79]. For densities closer to the 1.8 g/cm^3 measured by EDS, the observed stiffness and thermal conductivity would require a significantly lower porosity. Even though nanoporous materials display a reduction in thermal conductivity relative to bulk conditions, this effect is not expected to be dramatic in amorphous structures, which do not display strong ballistic thermal transport effects. As a reference, the traditional volume reduction effect on conductivity according to the models of Eucken and Russell [88,89] predicts an ∼2/3 reduction in thermal conductivity assuming 50% porosity. Using the conductivity bound established in Sec. V, this implies that the intrinsic conductivity of the amorphous carbon would be necessarily larger than 3.3 W/(m K), in good agreement with the bulk forms of diamondlike amorphous carbon shown in Fig. 6(a).

The elastic and thermal properties of the amorphous carbon layer could be modified due to the sub-20-nm thickness and bonding to the stiffer diamond substrate. While EUV scatterometry can extract mechanical properties of ultrathin films independent of substrate influence, recent theoretical and experimental work has shown that the presence of interfaces significantly impacts the mechanical properties of ultrathin films as the few near-surface atomic layers—which constitute a significant proportion of the total film volume—exhibit a different Young's modulus than those in the bulk

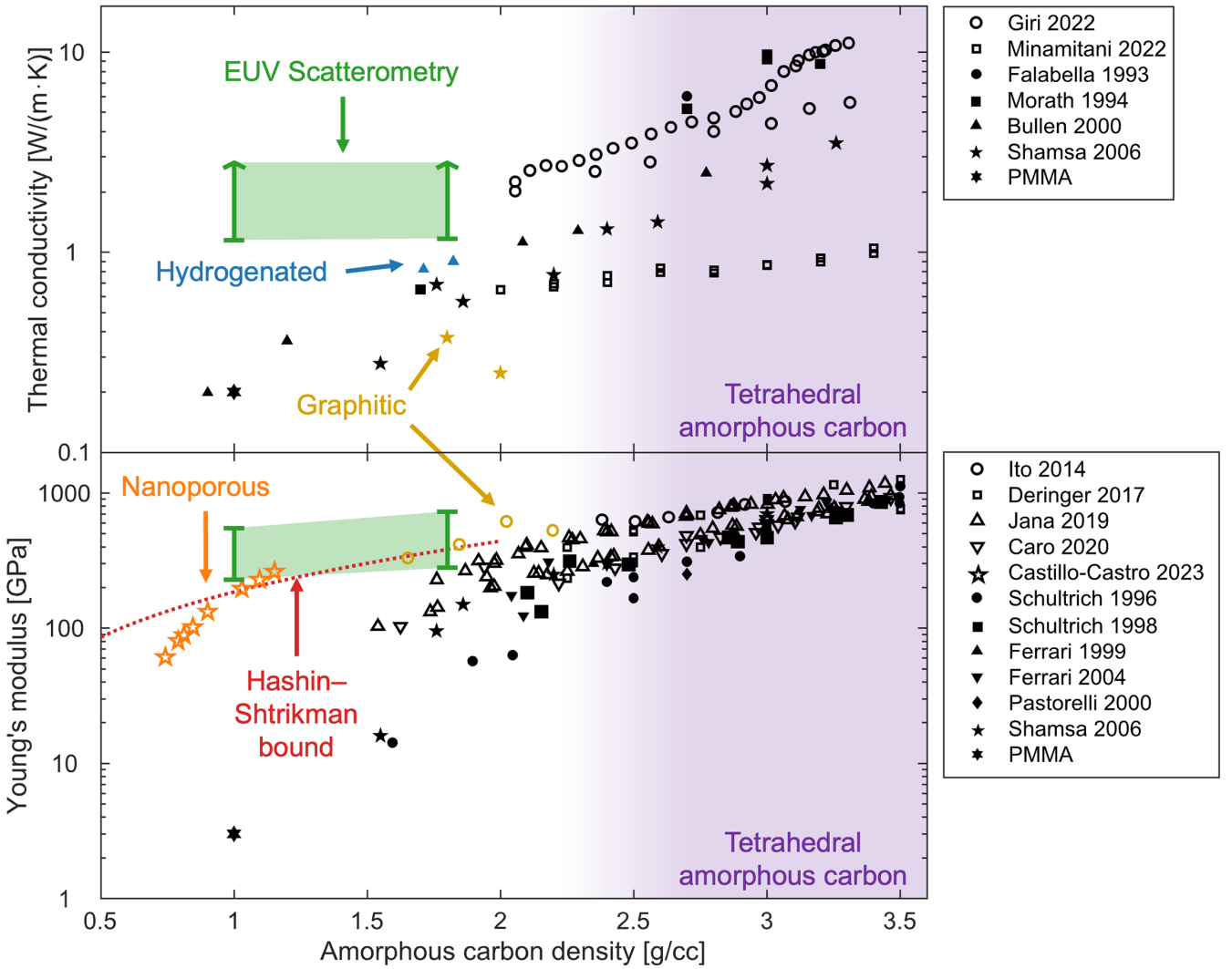

FIG. 6. Amorphous carbon characterized in this work compared to previous theoretical and experimental studies. (a) Thermal conductivity vs density, with data from Refs. [34–36,73–75]. The green shaded region interpolates between two analyses of the EUV scatterometry data, which assume densities of 1.0 and 1.8 g/cm^3 from the EUV imaging reflectometry and EDS measurements, respectively. The lower bound of the green shaded region is obtained assuming the minimum thermal boundary resistance of 0.3 nK m^2/W for the nickel-substrate interface, as given by Eq. (1). The top of the green shaded region is an orientative value assuming a TBR of 3.3 nK m^2/W, based on past experimental measurements [70]. Blue triangles and gold stars correspond to prior experimental measurements of hydrogenated amorphous carbon with a higher sp^3 ratio and graphitic amorphous carbon with a lower sp^3 ratio, respectively [35,36]. (b) Young's modulus vs density, with data from Refs. [30–33,36,71,76–80]. The green shaded region illustrates the error bars on the EUV scatterometry analysis discussed in SM Sec. VI [44]. Orange stars and gold circles correspond to prior simulations of nanoporous amorphous carbon and nonporous, graphitic, amorphous carbon, respectively [71,79]. The dotted red line gives the Hashin-Shtrikman upper bound on the Young's modulus of a macroscale porous medium assuming diamond as the constituent material. The purple shaded region indicates the typical density range for nonporous, hydrogen-free tetrahedral amorphous carbons, with sp^3 ratios >50%.

[90–93]. In our case, the smooth transition between amorphous carbon and the underlying diamond apparent in the electron microscopy could further result in a different Young's modulus than if the material were to appear in bulk form, analogous to the observations of Hoogeboom-Pot *et al.*, where few-nanometer tantalum layers exhibited a 25% increase in the acoustic wave speed when bonded to nickel [42].

VII. CONCLUSION

The consistent appearance of an ultrathin amorphous carbon layer at metal-diamond interfaces after electron-beam lithography processes masks the advantageous optical, thermal, and electronic properties of the diamond substrate and illustrates the fabrication and metrology challenges of harnessing diamond's advantageous material properties in quantum and nanoelectronic devices. Nondestructive extreme ultraviolet metrology techniques, applied alongside traditional electron microscopy tools, enable a thorough characterization of the surprising properties of this layer. Dynamic EUV scatterometry reveals a high Young's modulus and thermal conductivity consistent with diamondlike forms of amorphous carbon with high sp^3 ratios, while EUV imaging reflectometry and energy-dispersive x-ray spectroscopy measurements

indicate a low density in the range of 1–2 g/cm^3. The surprisingly low density is consistent with the presence of nanometer or subnanometer voids and vacancies in a stiff and conductive constituent material. The lithographic origin and novel material properties of this amorphous carbon layer can inform computational simulations and *ab initio* investigations of carbon-based materials, as well as practical interface design in future diamond devices.

ACKNOWLEDGMENTS

The authors acknowledge support from the STROBE National Science Foundation Science & Technology Center, Grant No. DMR-1548924. We also acknowledge support from the National Science Foundation under Grant No. DMR-2117903 and support from the Facility for Electron Microscopy of Materials (CUFEMM, RRID: SCR_019306). Albert Beardo acknowledges support from the Spanish Ministry of Universities through a Margarita Salas fellowship funded by the European Union-NextGenerationEU. This research was supported in part by the Colorado Shared Instrumentation in Nanofabrication and Characterization (COSINC): the COSINC-CHR (Characterization) and CONSINC-FAB (Fabrication), College of Engineering & Applied Science, University of Colorado Boulder. The authors would like to acknowledge the support of the staff Tomoko Borsa and Dylan Bartusiak and the facility that have made this work possible.

H.K. is partially employed by KM Labs, the company which manufactured the Ti:sapphire amplifier used in this work.

[1] R. J. Warzoha, A. A. Wilson, B. F. Donovan, N. Donmezer, A. Giri, P. E. Hopkins, S. Choi, D. Pahinkar, J. Shi, S. Graham, Z. Tian, and L. Ruppalt, Applications and impacts of nanoscale thermal transport in electronics packaging, J. Electron. Packag. **143**, 020804 (2021).

[2] D. Araujo, M. Suzuki, F. Lloret, G. Alba, and P. Villar, Diamond for electronics: Materials, processing and devices, Materials **14**, 7081 (2021).

[3] M. Tordjman, Diamond electronics with high carrier mobilities, Nat. Electron. **5**, 21 (2022).

[4] C. J. Wort and R. S. Balmer, Diamond as an electronic material, Mater. Today **11**, 22 (2008).

[5] M. W. Geis, T. C. Wade, C. H. Wuorio, T. H. Fedynyshyn, B. Duncan, M. E. Plaut, J. O. Varghese, S. M. Warnock, S. A. Vitale, and M. A. Hollis, Progress toward diamond power field-effect transistors, Phys. Status Solidi A **215**, 1800681 (2018).

[6] Y. Sasama, T. Kageura, M. Imura, K. Watanabe, T. Taniguchi, T. Uchihashi, and Y. Takahide, High-mobility p-channel wide-bandgap transistors based on hydrogen-terminated diamond/hexagonal boron nitride heterostructures, Nat. Electron. **5**, 37 (2021).

[7] F. Lenzini, N. Gruhler, N. Walter, and W. H. P. Pernice, Integrated quantum photonic circuits made from diamond, in *Diamond for Quantum Applications Part 2*, edited by C. E. Nebel, I. Aharonovich, N. Mizuochi, and M. Hatano, Semiconductors and Semimetals Vol. 104 (Elsevier, New York, 2021), pp. 149–171.

[8] R. Schirhagl, K. Chang, M. Loretz, and C. L. Degen, Nitrogen-vacancy centers in diamond: Nanoscale sensors for physics and biology, Annu. Rev. Phys. Chem. **65**, 83 (2014).

[9] H. Bernien, L. Childress, L. Robledo, M. Markham, D. Twitchen, and R. Hanson, Two-photon quantum interference from separate nitrogen vacancy centers in diamond, Phys. Rev. Lett. **108**, 043604 (2012).

[10] A. Sipahigil, M. L. Goldman, E. Togan, Y. Chu, M. Markham, D. J. Twitchen, A. S. Zibrov, A. Kubanek, and M. D. Lukin, Quantum interference of single photons from remote nitrogen-vacancy centers in diamond, Phys. Rev. Lett. **108**, 143601 (2012).

[11] G. D. Fuchs, G. Burkard, P. V. Klimov, and D. D. Awschalom, A quantum memory intrinsic to single nitrogen-vacancy centres in diamond, Nat. Phys. **7**, 789 (2011).

[12] T. Schröder, S. L. Mouradian, J. Zheng, M. E. Trusheim, M. Walsh, E. H. Chen, L. Li, I. Bayn, and D. Englund, Quantum nanophotonics in diamond, J. Opt. Soc. Am. B **33**, B65 (2016).

[13] D. Rani, O. R. Opaluch, and E. Neu, Recent advances in single crystal diamond device fabrication for photonics, sensing and nanomechanics, Micromachines **12**, 36 (2021).

[14] J. Tisler, G. Balasubramanian, B. Naydenov, R. Kolesov, B. Grotz, R. Reuter, J.-P. Boudou, P. A. Curmi, M. Sennour, A. Thorel, M. Börsch, K. Aulenbacher, R. Erdmann, P. R. Hemmer, F. Jelezko, and J. Wrachtrup, Fluorescence and spin properties of defects in single digit nanodiamonds, ACS Nano **3**, 1959 (2009).

[15] B. K. Ofori-Okai, S. Pezzagna, K. Chang, M. Loretz, R. Schirhagl, Y. Tao, B. A. Moores, K. Groot-Berning, J. Meijer, and C. L. Degen, Spin properties of very shallow nitrogen vacancy defects in diamond, Phys. Rev. B **86**, 081406(R) (2012).

[16] K. J. Brown, E. Chartier, E. M. Sweet, D. A. Hopper, and L. C. Bassett, Cleaning diamond surfaces using boiling acid treatment in a standard laboratory chemical hood, J. Chem. Health Saf. **26**, 40 (2019).

[17] P. Kirsch, M. B. Assouar, O. Elmazria, V. Mortet, and P. Alnot, 5 GHz surface acoustic wave devices based on aluminum nitride/diamond layered structure realized using electron beam lithography, Appl. Phys. Lett. **88**, 223504 (2006).

[18] C. Monachon and L. Weber, Influence of diamond surface termination on thermal boundary conductance between Al and diamond, J. Appl. Phys. **113**, 183504 (2013).

[19] J. Robertson, Diamond-like amorphous carbon, Mater. Sci. Eng., R **37**, 129 (2002).

[20] P. K. Chu and L. Li, Characterization of amorphous and nanocrystalline carbon films, Mater. Chem. Phys. **96**, 253 (2006).

[21] N. Ohtake, M. Hiratsuka, K. Kanda, H. Akasaka, M. Tsujioka, K. Hirakuri, A. Hirata, T. Ohana, H. Inaba, M. Kano, and H.

Saitoh, Properties and classification of diamond-like carbon films, Materials **14**, 315 (2021).

[22] P. J. Fallon, V. S. Veerasamy, C. A. Davis, J. Robertson, G. A. J. Amaratunga, W. I. Milne, and J. Koskinen, Properties of filtered-ion-beam-deposited diamondlike carbon as a function of ion energy, Phys. Rev. B **48**, 4777 (1993).

[23] R. Lossy, D. L. Pappas, R. A. Roy, J. P. Doyle, J. J. Cuomo, and J. Bruley, Properties of amorphous diamond films prepared by a filtered cathodic arc, Diamond Relat. Mater. **77**, 4750 (1995).

[24] S. Ravi, P. Silva, S. Xu, B. X. Tay, H. S. Tan, and W. I. Milne, Nanocrystallites in tetrahedral amorphous carbon films, Appl. Phys. Lett. **69**, 491 (1996).

[25] J. Schwan, S. Ulrich, H. Roth, H. Ehrhardt, S. R. P. Silva, J. Robertson, R. Samlenski, and R. Brenn, Tetrahedral amorphous carbon films prepared by magnetron sputtering and dc ion plating, J. Appl. Phys. **79**, 1416 (1996).

[26] M. Weiler, S. Sattel, T. Giessen, K. Jung, H. Ehrhardt, V. S. Veerasamy, and J. Robertson, Preparation and properties of highly tetrahedral hydrogenated amorphous carbon, Phys. Rev. B **53**, 1594 (1996).

[27] A. C. Ferrari, A. Libassi, B. K. Tanner, V. Stolojan, J. Yuan, L. M. Brown, S. E. Rodil, B. Kleinsorge, and J. Robertson, Density, sp^3 fraction, and cross-sectional structure of amorphous carbon films determined by x-ray reflectivity and electron energy-loss spectroscopy, Phys. Rev. B **62**, 11089 (2000).

[28] M. F. Toney and S. Brennan, Measurements of carbon thin films using x-ray reflectivity, J. Appl. Phys. **66**, 1861 (1989).

[29] M. Iwaki, Estimation of the atomic density of amorphous carbon using ion implantation, SIMS and RBS, Surf. Coat. Technol. **158-159**, 377 (2002).

[30] B. Schultrich, H.-J. Scheibe, G. Grandremy, D. Drescher, and D. Schneider, Elastic modulus as a measure of diamond likeness and hardness of amorphous carbon films, Diam. Relat. Mater. **5**, 914 (1996).

[31] B. Schultrich, H.-J. Scheibe, D. Drescher, and H. Ziegele, Deposition of superhard amorphous carbon films by pulsed vacuum arc deposition, Surf. Coat. Technol. **98**, 1097 (1998).

[32] A. C. Ferrari, J. Robertson, M. G. Beghi, C. E. Bottani, R. Ferulano, and R. Pastorelli, Elastic constants of tetrahedral amorphous carbon films by surface Brillouin scattering, Appl. Phys. Lett. **75**, 1893 (1999).

[33] R. Pastorelli, A. C. Ferrari, M. G. Beghi, C. E. Bottani, and J. Robertson, Elastic constants of ultrathin diamond-like carbon films, Diam. Relat. Mater. **9**, 825 (2000).

[34] C. J. Morath, H. J. Maris, J. J. Cuomo, D. L. Pappas, A. Grill, V. V. Patel, J. P. Doyle, and K. L. Saenger, Picosecond optical studies of amorphous diamond and diamondlike carbon: Thermal conductivity and longitudinal sound velocity, J. Appl. Phys. **76**, 2636 (1994).

[35] A. J. Bullen, K. E. O'Hara, D. G. Cahill, O. Monteiro, and A. von Keudell, Thermal conductivity of amorphous carbon thin films, J. Appl. Phys. **88**, 6317 (2000).

[36] M. Shamsa, W. L. Liu, A. A. Balandin, C. Casiraghi, W. I. Milne, and A. C. Ferrari, Thermal conductivity of diamond-like carbon films, Appl. Phys. Lett. **89**, 161921 (2006).

[37] M. G. Beghi, A. C. Ferrari, C. E. Bottani, A. Libassi, B. K. Tanner, K. B. Teo, and J. Robertson, Elastic constants and structural properties of nanometre-thick diamond-like carbon films, Diam. Relat. Mater. **11**, 1062 (2002).

[38] T. D. Frazer, J. L. Knobloch, K. M. Hoogeboom-Pot, D. Nardi, W. Chao, R. W. Falcone, M. M. Murnane, H. C. Kapteyn, and J. N. Hernandez-Charpak, Engineering nanoscale thermal transport: Size- and spacing-dependent cooling of nanostructures, Phys. Rev. Appl. **11**, 024042 (2019).

[39] M. Tanksalvala *et al.*, Nondestructive, high-resolution, chemically specific 3D nanostructure characterization using phase-sensitive EUV imaging reflectometry, Sci. Adv. **7**, eabd9667 (2021).

[40] Y. Esashi, N. W. Jenkins, Y. Shao, J. M. Shaw, S. Park, M. M. Murnane, H. C. Kapteyn, and M. Tanksalvala, Tabletop extreme ultraviolet reflectometer for quantitative nanoscale reflectometry, scatterometry, and imaging, Rev. Sci. Instrum. **94**, 123705 (2023).

[41] R. I. Tobey, M. E. Siemens, O. Cohen, M. M. Murnane, H. C. Kapteyn, and K. A. Nelson, Ultrafast extreme ultraviolet holography: Dynamic monitoring of surface deformation, Opt. Lett. **32**, 286 (2007).

[42] K. M. Hoogeboom-Pot, E. Turgut, J. N. Hernández-Charpak, J. M. Shaw, H. C. Kapteyn, M. M. Murnane, and D. Nardi, Nondestructive measurement of the evolution of layer-specific mechanical properties in sub-10 nm bilayer films, Nano Lett. **16**, 4773 (2016).

[43] J. N. Hernández-Charpak, K. M. Hoogeboom-Pot, Q. Li, T. D. Frazer, J. L. Knobloch, M. Tripp, S. W. King, E. H. Anderson, W. Chao, M. M. Murnane, H. C. Kapteyn, and D. Nardi, Full characterization of the mechanical properties of 11–50 nm ultrathin films: Influence of network connectivity on the Poisson's ratio, Nano Lett. **17**, 2178 (2017).

[44] See Supplemental Material at http://link.aps.org/supplemental/10.1103/PhysRevMaterials.8.096001 for information on the sample fabrication, XRR and EDS measurements, modeling parameters, analysis of the EUV imaging reflectometry and scatterometry measurements, and error analysis. The Supplemental Material also contains Refs. [94–124].

[45] D. Shindo, T. Musashi, Y. Ikematsu, Y. Murakami, N. Nakamura, and H. Chiba, Characterization of DLC films by EELS and electron holography, J. Electron Microsc. **54**, 11 (2005).

[46] V. Serin, E. Beche, R. Berjoan, D. Dorignac, D. Rats, J. Fontaine, L. Vandenbulcke, C. Germain, and A. Catherinot, XAES, XPS, EELS and Raman spectroscopy of polycrystalline to amorphous films with various sp^2 to sp^3 bondings, in *Proceedings of the Fifth International Symposium on Diamond Materials*, edited by J. L. Davidson, W. D. Brown, A. Gicquel, B. V. Spitsyn, and J. C. Angus (The Electrochemical Society, Pennington, NJ, 1998), pp. 126–141.

[47] 10.5281/zenodo.592838.

[48] A. J. Papworth, C. J. Kiely, A. P. Burden, S. R. P. Silva, and G. A. J. Amaratunga, Electron-energy-loss spectroscopy characterization of the sp^2 bonding fraction within carbon thin films, Phys. Rev. B **62**, 12628 (2000).

[49] S. Döring, F. Hertlein, A. Bayer, and K. Mann, EUV reflectometry for thickness and density determination of thin film coatings, Appl. Phys. A **107**, 795 (2012).

[50] D. Sayre, Some implications of a theorem due to Shannon, Acta Cryst. **5**, 843 (1952).

[51] J. R. Fienup, Phase retrieval algorithms: A comparison, Appl. Opt. **21**, 2758 (1982).
[52] A. Maiden, D. Johnson, and P. Li, Further improvements to the ptychographical iterative engine, Optica **4**, 736 (2017).
[53] A. Rundquist III, C. G. Durfee, Z. Chang, C. Herne, S. Backus, M. M. Murnane, and H. C. Kapteyn, Phase-matched generation of coherent soft X-rays, Science **280**, 1412 (1998).
[54] L. G. Parratt, Surface studies of solids by total reflection of x-rays, Phys. Rev. **95**, 359 (1954).
[55] A. D. Dane, A. Veldhuis, D. K. G. Boer, A. J. G. Leenaers, and L. M. C. Buydens, Application of genetic algorithms for characterization of thin layered materials by glancing incidence x-ray reflectometry, Phys. B (Amsterdam, Neth.) **253**, 254 (1998).
[56] A. Ulyanenkov, K. Omote, and J. Harada, The genetic algorithm: Refinement of x-ray reflectivity data from multilayers and thin films, Phys. B (Amsterdam, Neth.) **283**, 237 (2000).
[57] W. H. Press, S. A. Teukosky, W. T. Vetterling, and B. P. Flannery, Modeling of data, in *Numerical Recipes: The Art of Scientific Computing*, 3rd ed. (Cambridge University Press, Cambridge, 2007), pp. 773–839.
[58] COMSOL AB, Stockholm, Sweden, Comsol multiphysics® v. 5.3a.
[59] D. Nardi, F. Banfi, C. Giannetti, B. Revaz, G. Ferrini, and F. Parmigiani, Pseudosurface acoustic waves in hypersonic surface phononic crystals, Phys. Rev. B **80**, 104119 (2009).
[60] D. Nardi, M. Travagliati, M. E. Siemens, Q. Li, M. M. Murnane, H. C. Kapteyn, G. Ferrini, F. Parmigiani, and F. Banfi, Probing thermomechanics at the nanoscale: Impulsively excited pseudosurface acoustic waves in hypersonic phononic crystals, Nano Lett. **11**, 4126 (2011).
[61] X. Jiang, K. Reichelt, and B. Stritzker, Mechanical properties of a-C:H films prepared by plasma decomposition of C_2H_2, J. Appl. Phys. **68**, 1018 (1990).
[62] J. R. Cost, K. R. Janowski, and R. C. Rossi, Elastic properties of isotropic graphite, Philos. Mag. A **17**, 851 (1968).
[63] C. A. Klein and G. F. Cardinale, Young's modulus and Poisson's ratio of CVD diamond, Diamond Relat. Mater. **2**, 918 (1993).
[64] F. Dalla Longa, J. T. Kohlhepp, W. J. M. de Jonge, and B. Koopmans, Influence of photon angular momentum on ultrafast demagnetization in nickel, Phys. Rev. B **75**, 224431 (2007).
[65] W. Li, N. Mingo, L. Lindsay, D. A. Broido, D. A. Stewart, and N. A. Katcho, Thermal conductivity of diamond nanowires from first principles, Phys. Rev. B **85**, 195436 (2012).
[66] P. Patsalas, Optical properties of amorphous carbons and their applications and perspectives in photonics, Thin Solid Films **519**, 3990 (2011).
[67] A. Giri and P. E. Hopkins, A review of experimental and computational advances in thermal boundary conductance and nanoscale thermal transport across solid interfaces, Adv. Funct. Mater. **30**, 1903857 (2020).
[68] E. T. Swartz and R. O. Pohl, Thermal boundary resistance, Rev. Mod. Phys. **61**, 605 (1989).
[69] R. B. Wilson, B. A. Apgar, W.-P. Hsieh, L. W. Martin, and D. G. Cahill, Thermal conductance of strongly bonded metal-oxide interfaces, Phys. Rev. B **91**, 115414 (2015).
[70] M. Blank and L. Weber, Towards a coherent database of thermal boundary conductance at metal/dielectric interfaces, J. Appl. Phys. **125**, 095302 (2019).
[71] A. M. Ito, A. Takayama, Y. Oda, and H. Nakamura, The first principle calculation of bulk modulus and Young's modulus for amorphous carbon material, J. Phys.: Conf. Ser. **518**, 012011 (2014).
[72] Y. Yang, C.-C. Chen, M. Scott, C. Ophus, R. Xu, A. Pryor, L. Wu, F. Sun, W. Theis, J. Zhou, M. Eisenbach, P. R. Kent, R. F. Sabrianov, H. Zeng, P. Ercius, and J. Miao, Deciphering chemical order/disorder and material properties at the single-atom level, Nature (London) **542**, 75 (2017).
[73] A. Giri, C. Dionne, and P. Hopkins, Atomic coordination dictates vibrational characteristics and thermal conductivity in amorphous carbon, npj Comput. Mater. **8**, 55 (2022).
[74] E. Minamitani, T. Shiga, M. Kashiwagi, and I. Obayashi, Relationship between local coordinates and thermal conductivity in amorphous carbon, J. Vac. Sci. Technol. A **40**, 033408 (2022).
[75] S. Falabella, D. Boercker, and D. Sanders, Fabrication of amorphous diamond films, Thin Solid Films **236**, 82 (1993).
[76] V. L. Deringer and G. Csányi, Machine learning based interatomic potential for amorphous carbon, Phys. Rev. B **95**, 094203 (2017).
[77] R. Jana, D. Savio, V. L. Deringer, and L. Pastewka, Structural and elastic properties of amorphous carbon from simulated quenching at low rates, Modell. Simul. Mater. Sci. Eng. **27**, 085009 (2019).
[78] M. A. Caro, G. Csányi, T. Laurila, and V. L. Deringer, Machine learning driven simulated deposition of carbon films: From low-density to diamondlike amorphous carbon, Phys. Rev. B **102**, 174201 (2020).
[79] D. Castillo-Castro, F. Correa, E. Aparicio, N. Amigo, A. Prada, J. Figueroa, R. I. González, E. Bringa, and F. J. Valencia, Nanoporous amorphous carbon with exceptional ultra-high strength, Nanomaterials **13**, 1429 (2023).
[80] A. C. Ferrari, Diamond-like carbon for magnetic storage disks, Surf. Coat. Technol. **180-181**, 190 (2004).
[81] J. Bauer, A. Schroer, R. Schwaiger, and O. Kraft, Approaching theoretical strength in glassy carbon nanolattices, Nat. Mater. **15**, 438 (2016).
[82] X. Chen, G. Zhao, Y. Wu, Y. Huang, Y. Liu, J. He, L. Wang, Q. Lian, and D. Li, Cellular carbon microstructures developed by using stereolithography, Carbon **123**, 34 (2017).
[83] C. Crook, J. Bauer, A. Guell-Izard, C. Santos de Oliveira, J. Martins de Souza e Silva, J. Berger, and L. Valdevit, Plate-nanolattices at the theoretical limit of stiffness and strength, Nat. Commun. **11**, 1579 (2020).
[84] Z. Hashin and S. Shtrikman, A variational approach to the theory of the elastic behaviour of multiphase materials, J. Mech. Phys. Solids **11**, 127 (1963).
[85] N. A. Marks, Generalizing the environment-dependent interaction potential for carbon, Phys. Rev. B **63**, 035401 (2000).
[86] N. A. Marks, N. C. Cooper, D. R. McKenzie, D. G. McCulloch, P. Bath, and S. P. Russo, Comparison of density-functional, tight-binding, and empirical methods for the simulation of amorphous carbon, Phys. Rev. B **65**, 075411 (2002).
[87] B. Bhattarai and D. Drabold, Amorphous carbon at low densities: An ab initio study, Carbon **115**, 532 (2017).

[88] D. Song and G. Chen, Thermal conductivity of periodic microporous silicon films, Appl. Phys. Lett. **84**, 687 (2004).

[89] H. W. Russell, Principles of heat flow in porous insulators, J. Am. Ceram. Soc. **18**, 1 (1935).

[90] T. D. Frazer, J. L. Knobloch, J. N. Hernández-Charpak, K. M. Hoogeboom-Pot, D. Nardi, S. Yazdi, W. Chao, E. H. Anderson, M. K. Tripp, S. W. King, H. C. Kapteyn, M. M. Murnane, and B. Abad, Full characterization of ultrathin 5-nm low-k dielectric bilayers: Influence of dopants and surfaces on the mechanical properties, Phys. Rev. Mater. **4**, 073603 (2020).

[91] A. I. Fedorchenko, A. B. Wang, and H. H. Cheng, Thickness dependence of nanofilm elastic modulus, Appl. Phys. Lett. **94**, 152111 (2009).

[92] J. Lian, S. W. Lee, L. Valdevit, M. I. Baskes, and J. R. Greer, Emergence of film-thickness- and grain-size-dependent elastic properties in nanocrystalline thin films, Scr. Mater. **68**, 261 (2013).

[93] B. Gong, Q. Chen, and D. Wang, Molecular dynamics study on size-dependent elastic properties of silicon nanoplates, Mater. Lett. **67**, 165 (2012).

[94] J. Hollenshead and L. Klebanoff, Modeling radiation-induced carbon contamination of extreme ultraviolet optics, J. Vac. Sci. Technol. B **24**, 64 (2006).

[95] D. E. Newbury, C. R. Swyt, and R. L. Myklebust, "Standardless" quantitative electron probe microanalysis with energy-dispersive x-ray spectrometry: Is it worth the risk? Anal. Chem. **67**, 1866 (1995).

[96] A. Champi, R. Lacerda, G. Viana, and F. Marques, Thermal expansion dependence on the sp^2 concentration of amorphous carbon and carbon nitride, J. Non-Cryst. Solids **338-340**, 499 (2004).

[97] I. Mori, O. Suga, H. Tanaka, I. Nishiyama, T. Terasawa, H. Shigemura, T. Taguchi, T. Tanaka, and T. Itani, Selete's EUV program: progress and challenges, in *Emerging Lithographic Technologies XII*, edited by F. M. Schellenberg, International Society for Optics and Photonics (SPIE, Bellingham, Washington, 2008), Vol. 6921, p. 692102.

[98] Y. Nishiyama, T. Anazawa, H. Oizumi, I. Nishiyama, O. Suga, K. Abe, S. Kagata, and A. Izumi, Carbon contamination of EUV mask: film characterization, impact on lithographic performance, and cleaning, in *Emerging Lithographic Technologies XII*, edited by F. M. Schellenberg, International Society for Optics and Photonics (SPIE, Bellingham, Washington, 2008), Vol. 6921, p. 692116.

[99] D. R. Lide, *CRC Handbook of Chemistry and Physics*, 85th ed. (CRC Press, Boca Raton, FL, 2005).

[100] J. Dean and N. Lange, *Lange's Handbook of Chemistry*, 15th ed. (McGraw-Hill, New York, 1999).

[101] J. Keem and J. Honig, Selected Electrical and Thermal Properties of Undoped Nickel Oxide, Technical Report No. ADA128940, Thermophysical and Eletronic Properties Information Analysis Center, Lafayette, Indiana, 1978.

[102] J. Chen, E. Louis, H. Wormeester, R. Harmsen, R. van de Kruijs, C. J. Lee, W. van Schaik, and F. Bijkerk, Carbon-induced extreme ultraviolet reflectance loss characterized using visible-light ellipsometry, Meas. Sci. Technol. **22**, 105705 (2011).

[103] T. G. Kollie, Measurement of the thermal-expansion coefficient of nickel from 300 to 1000 K and determination of the power-law constants near the Curie temperature, Phys. Rev. B **16**, 4872 (1977).

[104] F. Banfi, F. Pressacco, B. Revaz, C. Giannetti, D. Nardi, G. Ferrini, and F. Parmigiani, *Ab initio* thermodynamics calculation of all-optical time-resolved calorimetry of nanosize systems: Evidence of nanosecond decoupling of electron and phonon temperatures, Phys. Rev. B **81**, 155426 (2010).

[105] S. Stoupin and Y. V. Shvyd'ko, Ultraprecise studies of the thermal expansion coefficient of diamond using backscattering x-ray diffraction, Phys. Rev. B **83**, 104102 (2011).

[106] H. Watanabe, Thermal constants for Ni, NiO, MgO, MnO and CoO at low temperatures, Thermochim. Acta **218**, 365 (1993).

[107] I. Fasaki, A. Koutoulaki, M. Kompitsas, and C. Charitidis, Structural, electrical and mechanical properties of NiO thin films grown by pulsed laser deposition, Appl. Surf. Sci. **257**, 429 (2010).

[108] H. Chen, H. Ma, Y. Zhu, M. Zhao, Z. Chen, and L. Zhang, Novel approach for improving electrochromic and mechanical properties of NiO film: Experiment and molecular dynamics simulation, Appl. Surf. Sci. **609**, 155209 (2023).

[109] E. R. Shanblatt, Jr., C. L. Porter, D. F. Gardner, G. F. Mancini, R. M. Karl, Jr., M. D. Tanksalvala, C. S. Bevis, V. H. Vartanian, H. C. Kapteyn, D. E. Adams, and M. M. Murnane, Quantitative chemically specific coherent diffractive imaging of reactions at buried interfaces with few nanometer precision, Nano Lett. **16**, 5444 (2016).

[110] D. F. Gardner, M. Tanksalvala, E. R. Shanblatt, X. Zhang, B. R. Galloway, C. L. Porter, R. Karl, Jr., C. Bevis, D. E. Adams, H. C. Kapteyn, M. M. Murnane, and G. F. Mancini, Subwavelength coherent imaging of periodic samples using a 13.5 nm tabletop high-harmonic light source, Nat. Photon. **11**, 259 (2017).

[111] P. Thibault and A. Menzel, Reconstructing state mixtures from diffraction measurements, Nature (London) **494**, 68 (2013).

[112] D. F. Gardner, B. Zhang, M. D. Seaberg, L. S. Martin, D. E. Adams, F. Salmassi, E. Gullikson, H. Kapteyn, and M. Murnane, High numerical aperture reflection mode coherent diffraction microscopy using off-axis apertured illumination, Opt. Express **20**, 19050 (2012).

[113] C. L. Porter, M. Tanksalvala, M. Gerrity, G. Miley, X. Zhang, C. Bevis, E. Shanblatt, R. Karl, M. M. Murnane, D. E. Adams, and H. C. Kapteyn, General-purpose, wide field-of-view reflection imaging with a tabletop 13 nm light source, Optica **4**, 1552 (2017).

[114] J. T. Hollenshead, L. E. Klebanoff, and G. Delgado, Predicting radiation-induced carbon contamination of EUV optics, J. Vac. Sci. Technol. B **37**, 021602 (2019).

[115] L. Névot and P. Croce, Caractérisation des surfaces par réflexion rasante de rayons X. Application à l'étude du polissage de quelques verres silicates, Rev. Phys. Appl. **15**, 761 (1980).

[116] D. Attwood and A. Sakdinawat, Wave propagation and refractive index at x-ray and EUV wavelengths, in *X-Rays and Extreme Ultraviolet Radiation*, 2nd ed. (Springer, New York, 2016), pp. 60–109.

[117] Y. Esashi, M. Tanksalvala, Z. Zhang, N. W. Jenkins, H. C. Kapteyn, and M. M. Murnane, Influence of surface and interface roughness on x-ray and extreme ultraviolet reflectance: A comparative numerical study, OSA Continuum **4**, 1497 (2021).

[118] D. J. Batey, D. Claus, and J. M. Rodenburg, Information multiplexing in ptychography, Ultramicroscopy **138**, 13 (2014).

[119] B. Henke, E. Gullikson, and J. Davis, X-ray interactions: Photoabsorption, scattering, transmission, and reflection at $E =$ 50-30,000 eV, $Z =$ 1-92, At. Data Nucl. Data Tables **54**, 181 (1993).

[120] M. I. Kaganov, I. M. Lifshitz, and L. V. Tanatarov, Relaxation between electrons and the crystalline lattice, Sov. Phys. JETP **4**, 173 (1957).

[121] J. L. Knobloch, New Understanding of Nanoscale Thermal Transport and Mechanical Properties Uncovered Using Coherent Extreme Ultraviolet Light, PhD. thesis, University of Colorado at Boulder, 2020.

[122] B. McBennett, A. Beardo, E. E. Nelson, B. Abad, T. D. Frazer, A. Adak, Y. Esashi, B. Li, H. C. Kapteyn, M. M. Murnane, and J. L. Knobloch, Universal behavior of highly confined heat flow in semiconductor nanosystems: From nanomeshes to metalattices, Nano Lett. **23**, 2129 (2023).

[123] W. Jifang, E. S. Fisher, and M. H. Manghnzmi, Elastic constants of nickel oxide, Chin. Phys. Lett. **8**, 153 (1991).

[124] A. Beardo, J. L. Knobloch, L. Sendra, J. Bafaluy, T. D. Frazer, W. Chao, J. N. Hernández-Charpak, H. C. Kapteyn, B. Abad, M. M. Murnane, F. X. Alvarez, and J. Camacho, A general and predictive understanding of thermal transport from 1D-and 2D-confined nanostructures: Theory and experiment, ACS Nano **15**, 13019 (2021).